Journal of Materials Chemistry A

Materials for energy and sustainability

rsc.li/materials-a

ROYAL SOCIETY
OF **CHEMISTRY**

PAPER
Jeroni Morey, Antonio Bauzá *et al.*
Capturing volatile organic compounds using Ag and Au
nanoparticles: regium–π and C–H···Ag/Au interactions
at work

10 YEARS
ANNIVERSARY

Check for updates

Capturing volatile organic compounds using Ag and Au nanoparticles: regium–π and C–H⋯Ag/Au interactions at work†

Maria de las Nieves Piña, Jeroni Morey, [ID] * Antonio Frontera [ID] and Antonio Bauzá [ID] *

Volatile Organic Compounds (VOCs) are chemicals that vaporize at room temperature and exert short- or long-term adverse effects on human health and the environment. In this study, Ag and Au nanoparticles (NPs) were used to capture aromatic VOCs (*e.g.* benzene derivatives) through the establishment of CH⋯Ag/Au interactions and regium–π bonds (Rg–π), namely, an attractive noncovalent force involving low electron density sites located on noble metal NPs acting as electron acceptors and π-systems as electron donors. Using a set of computational tools (PBE0-D3/def2-TZVP level of theory), we modeled the interaction between the VOCs and the Ag/Au NPs, being useful to understand its strength and physical nature. On the other hand, thermal desorption (TD) experiments evidenced the presence of a noncovalent interaction between the surface of the NPs and VOCs that drives the molecular recognition process, in line with the results gathered from calculations. We believe the results gathered herein will be useful (i) to bring the attention of the materials science community to this novel type of noncovalent force, (ii) to expand the current knowledge and usage of Ag and Au NPs and (iii) to develop new nanoscale materials for capturing volatile compounds.

Introduction

In a daily basis, we are constantly surrounded by a myriad of chemical substances, which exert profound effects on our health and the environment.[1] Among them, Volatile Organic Compounds (VOCs) encompass a large group of carbon-based chemicals that evaporate at room temperature and are present in a variety of products, materials, and everyday items.[2–4] VOCs are released into the air through natural processes, such as those related to plant and animal metabolism,[5–7] thus playing an essential role in biological and geological cycles. For instance, plants release VOCs as part of their defense mechanisms or for attracting pollinators, as well as to communicate with other organisms.[5] On the other hand, different types of VOCs are generated as a consequence of industrial processes[8] (such as solvents or intermediates from chemical reactions), raw materials for the production of casual items (*e.g.* paints, adhesives and cleaning agents), transportation,[9] and the use of consumer products,[10] being considered as a high priority targets to prevent environmental and human health degradation.[1,11,12]

In this context, one of the primary sources of VOC emissions is the combustion of fossil fuels,[13–15] which releases volatile hydrocarbons into the atmosphere. Motor vehicles, power plants, and industrial facilities are major contributors to VOC emissions, leading to the formation of ground-level ozone and the creation of smog, particularly in urban areas.[16,17] Consequently, severe effects on human health are exerted, including respiratory issues, eye irritation, and increased vulnerability to respiratory infections.[18]

Furthermore, VOCs can dramatically affect the natural environment and wildlife by contaminating soil and water sources, thus disrupting the delicate balance of ecosystems and potentially harming plants, animals, and aquatic organisms,[19] leading to a loss of biodiversity and pose long-term ecological challenges (see Fig. 1).

In this regard, Governments and regulatory agencies have implemented guidelines and standards to limit VOC emissions from industries and consumer products,[20–22] while technological advancements and research have led to the development of low-VOC or zero-VOC alternatives, promoting environmentally friendly practices, and reducing exposure to these harmful compounds. Despite this, efforts continue in the development of feasible alternatives to efficiently capture and retain VOCs, being of paramount importance for both human health and the environment.

In this work we have combined theoretical approaches (calculations at the PBE0-D3/def2-TZVP level of theory) with

Department of Chemistry, Universitat de les Illes Balears, Ctra. de Valldemossa km 7.5, Baleares, 07122, Palma, Spain. E-mail: jeroni.morey@uib.es; antonio.bauza@uib.es; Fax: +34 971 173426

This journal is © The Royal Society of Chemistry 2023

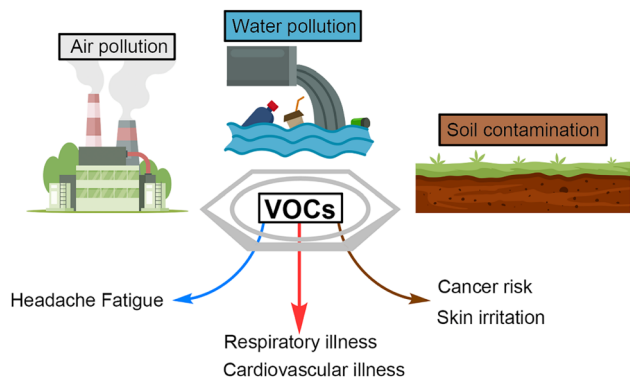*J. Mater. Chem. A*, 2023, 11, 25865–25874 | **25865**

Fig. 1 Schematic representation of the VOC accumulation in different environments (air, water, and soil) (top) and their impact in our health (bottom).

thermal desorption (TD) experiments to understand the molecular recognition process between several known VOCs and Ag and Au nanoparticles (NPs). More in detail, we have used Ag282 and Au282 NPs as computational models and evaluated the strength and physical nature of the Rg–π interaction between the NPs and several VOCs (benzene, toluene, o-xylene, m-xylene, p-xylene, 1,2,3-trimethylbenzene, 1,3,5-trifluorobenzene and hexafluorobenzene molecules). This was carried out by using state of the art computational techniques such as the Molecular Electrostatic Potential (MEP) surface analysis, useful to account for the electrostatics of the interaction, the "Atoms in Molecules" (AIM) and Non Covalent Interaction plot (NCIplot) methodologies, which shed light into the relative strength of the NCIs involved in the formation of the noncovalent complexes studied herein as well as their extension in real space. Additionally, the Energy Decomposition Analysis (EDA) was used to elucidate the energy components responsible for the stabilization of the VOCs over the metal layer as well as the Natural Bonding Orbital (NBO) analysis, which accounted for the presence of orbital interactions between the VOCs and the metal NPs.

As a result of the theoretical modeling phase, we observed that the absorption of the VOC over the metal NP was mainly driven by the formation of a regium bond in combination with C–H⋯Ag/Au interactions, which might be understood as "unconventional" hydrogen bonds or dispersion-based interactions. Regium bonding interactions (also known as Coinage bonds) have been described in the literature as an attractive noncovalent force involving low electron density sites located on noble metal NPs and Lewis bases.[23–25] In the case that the Lewis base is composed by a π-system, the interaction is described as a regium–π bond (Rg–π).[26]

Bearing this in mind, TD experiments have been carried out to evaluate the capturing and retaining process of the VOCs by Ag and Au NPs. Our group has experience with using absorbent nanomaterials to capture aromatic and non-aromatic VOCs by using hybrid nanoparticles based on magnetite covered by perilen-diimide (PDI), naftalen-diimide (NDI) and pyromellitic diimide (NPI),[27,28] with good adsorption percentages. TD is

a fast and clean technique that allows to evaluate in a reproducible and safe way the interaction capacity of the nanomaterial with the proposed analytes. In turn, it also allows checking the stability of the adsorbent material, since it is possible to carry out periodic tests of its interaction capacity.[28] Additionally, it has been determined that it is possible to reuse the nanomaterial, both AgNP and AuNP, up to a hundred times, without losing its adsorption capacity on the VOC analyzed.

The metal NPs used herein represent a good alternative to the previously used hybrid materials, since they require less synthesis time, thus reducing the number of reagents and energy used, which ultimately leads to a sustainable cycle of less pollution and consumption. Hence, we expect the results reported herein will be useful (i) to expand the current knowledge about regium–π bonds among the materials science community, (ii) to broad the current knowledge and usage of Ag and Au NPs and (iii) to develop novel nanoscale materials for capturing volatile compounds.

Methods

Computational methods

The interaction energies of all complexes included in this study were computed at the PBE0[29,30]-D3[31]/def2-TZVP[32] level of theory. The calculations have been performed using the program TURBOMOLE version 7.7.[33] More in detail, the Ag and Au layers were built using the geometries reported in the study of Sawabe and collaborators,[34] by slicing a portion of 26 atoms belonging to the 282 atom cluster (which corresponds to one of the "faces" of the metal decahedron structure). The metal layer was kept frozen while the VOC was left freely to explore the most favourable disposition over the Ag/Au layer. The interaction energies were calculated using the supermolecule approximation ($\Delta E = E_{\text{Ag/Au layer–VOC complex}} - E_{\text{VOC}} - E_{\text{Ag/Au layer}}$). The interaction energies gathered in Table 2 were corrected using the Boys and Bernardi counterpoise technique.[35] During the optimizations no symmetry was imposed on the system. The optimized structures do not correspond to fully relaxed geometries since we wanted to preserve the original geometry of the metal layer when extracted from the cluster, therefore frequency analysis calculations were not performed.

The MEP surfaces were computed at the PBE0/def2-TZVP level of theory by means of the Gaussian 16 software[36] and analyzed using the Gaussview 5.0 program.[37] The calculations for the wavefunction analysis were also carried out at the PBE0/def2-TZVP level of theory (also using the Gaussian 16 software) and analyzed by means of the AIMall software.[38] The NBO[39] analyses were performed at the HF/def2-TZVP level of theory. In addition, the Energy Decomposition Analysis (EDA)[40,41] scheme was used to understand the role of electrostatics, exchange-repulsion, orbital, dispersion and electron correlation contributions in the formation of the noncovalent complexes studied herein at the PBE0-D3/def2-TZVP level of theory, also using TURBOMOLE 7.7 software.

Lastly, the NCIplot[42] isosurfaces correspond to both favorable and unfavorable interactions, as differentiated by the sign of the second-density Hessian eigenvalue and defined by the

25866 | *J. Mater. Chem. A*, 2023, **11**, 25865–25874

This journal is © The Royal Society of Chemistry 2023

isosurface color. The color scheme is a red–yellow–green–blue scale, with red for repulsive (ρ_{cut}^{+}) and blue for attractive (ρ_{cut}^{-}) NCI interaction density. Yellow and green surfaces correspond to weak repulsive and weak attractive interactions, respectively. The surfaces were visualized using the Visual Molecular Dynamics (VMD) software.[43]

Experimental methods

The nanoparticles are thermally stable up to 900 °C (see ESI, Fig. S1 and S4†), therefore they are suitable for utilization in the experiments detailed below, as the maximum temperature used in the different apparatus is 375 °C. No loss of adsorption capacity of the metal nanoparticles has been detected even after 100 repetitions of the experiment. The AgNO$_3$, the HAuCl$_4$·3H$_2$O, the NaBH$_4$, and the VOCs were purchased from Sigma-Aldrich and Fluka (Buchs, Switzerland). The VOCs purity was higher than 98% in all cases. The ethanol was purchased from Scharlab (Barcelona, Spain). The glass TD tubes (6 mm diameter and 90 mm length), commercial adsorbents, Carbotrap B®, Carbopack X®, Carboxen 565®, and the unsilanized glass wool were purchased from Supelco (Bellefonte, PA, USA).

Synthesis of the nanoparticles

AgNPs were synthesized by using a previously reported method.[44] This methodology was then adapted to obtain the AuNPs. Briefly, in a 100 mL round bottom flask, 10 mL of 1 M AgNO$_3$ in millipore water were introduced. Keeping this solution under constant stirring and in an ice-water bath, 30 mL of a 1.5 M sodium borohydride solution in millipore water were added very slowly, allowing the reaction to finish between additions. Once the addition is complete, the final mixture was left stirring in an ice-water bath for 1.5 hours. After this time, the appearance of the metallic gray solid can be seen. The nanoparticles are recovered by centrifugation at 6000 rpm for 5 min. The supernatant is separated, and the solid is washed with 6 mL of millipore water for 4 times. To carry out the washing correctly, 6 mL of water are added, the mixture is sonicated for 1 min and centrifuged at 6000 rpm for 5 min. Finally, two washes with 6 mL of ethanol are carried out in the same way, to facilitate drying of the nanoparticles. Once separated from the liquid, they are dried in the oven at 125 °C for 1 day. Thus, 995 mg of AgNPs are obtained, ready to be introduced into the TD test tubes. In the case of Au nanoparticles, a solution of 52.4 mg (0.133 mmol) of HAuCl$_4$·3H$_2$O in 50 mL of millipore water was used. During the addition of the NaBH$_4$ solution, the color variation of the solution can be observed, from dark red to bluish and finally bluish-black, due to the formation of AuNPs. After the washing and drying operations, 900 mg of a bright yellow-brown solid are obtained. Both nanoparticles were analyzed by TGA, SEM-EDX, TEM and DLS (see ESI, Fig. S1–S6†). In both cases, it was possible to verify that they did not have any surface coating, that they are stable up to at least 900 °C, and that their average size is 50 nm for AgNPs and 90 nm for AuNPs. Due to the lack of coating, the nanoparticles aggregate when in solution, as it can be seen in TEM micrographs.

Fabrication of the sorbent tubes and adsorption/desorption experiments

Since the purpose of this work was the study of the Rg–π interactions between the metallic nanoparticles and the selected VOCs, the experiments could not be carried out with a solvent, because it could distort the results. For this reason, it was not possible to obtain calibration plots to quantify the magnitude of the metal–VOC interaction. Instead, some tubes were prepared with a mixture of commercial absorbents (Carbotrap B®, Carbopack X®, Carboxen 565®), which are known to have some retention of these analytes.[45] Thus, the relative retention percentage for Ag and Au was calculated according to the area ratio of the chromatogram peaks.

Therefore, three types of tubes were prepared, one with Ag nanoparticles (220 mg, 2.03 mmol), another with Au nanoparticles (400 mg, 2.03 mmol) and another with commercial adsorbents (70 mg Carbotrap B®, 100 mg Carbopack X®, 90 mg Carboxen 565®, 260 mg), each one in triplicate to ensure the repeatability of the experiment (9 tubes in all). For each measurement with a single VOC, the 9 tubes are doped and analyzed in the same experiment, with an autosampler. The measurement is repeated on 3 different days. The final value is an average of all the results obtained for the same VOC and the same type of adsorbent.

The metallic nanoparticles were introduced in each tube and a periodical test was done to every tube to check that it was able to give the same analytical result when doped with the same quantity of a given VOC. After total desorption, a verification that both tubes are perfectly clean was carried out. Before the first use, a thermal cleaning was performed using the following protocol: 250 °C for 20 min, 300 °C for 20 min, 350 °C for 20 min and 375 °C for 20 min under a flow rate of dry N$_2$ of 70 mL min^{-1}. For successive experiments, pre-conditioning for 20 min at 375 °C was used. After conditioning, they were immediately sealed with Swagelock end caps fitted with PTFE ferrules and stored in closed plastic boxes filled with desiccant material. The commercial doping device supplied by the instrument manufacturer was employed for the doping of the tubes. A manual injection under a flow rate of dry N$_2$ of 100 mL min^{-1} of the VOC was carried out. This is done through a Swagelock adapter (stainless steel) that connects the tube without any possibility of leakage. The constant N$_2$ flow guarantees the homogeneity of the sample through the sorbent. For the sake of reproducibility, 1 μL of VOC was always used and a doping time of 5 min was applied. During the first minute, the syringe was kept in the injector to maintain the flux unperturbed.

Analytical instrumentation and procedure

The VOC analyses were carried out by using an autosampler (Ultra-xr) coupled to thermal desorption (TD) (Unity 2 model, Markes International) coupled to a gas chromatograph with an FID detector (6890A model, Agilent Technologies). The first step is an initial pre-desorption for 0.1 min and a flux of 20 mL min^{-1}. Subsequently, a primary desorption is performed at 300 °C for 10 min, with a split of 4 mL min^{-1}. During this period, the analyte that was previously adsorbed in the tube is

This journal is © The Royal Society of Chemistry 2023

J. Mater. Chem. A, 2023, **11**, 25865–25874 | **25867**

concentrated in a cryofocusing trap that contains 30 mg of Tenax TA, and is kept at −30 °C. Afterwards, the trap is quickly heated from −30 °C to 300 °C and kept at the final temperature for 10 min and, thus, the secondary desorption takes place. In this step, the analyte is sent to the gas chromatograph by using a split with a flux of 7 mL min^{-1} and finally injected into a capillary column (DB-624, 60 m × 0.25 mm × 1.4 mm, Agilent Technologies) through a line at 200 °C. The oven temperature was initially set at 40 °C for 1 min and progressively increased (rate of 6 °C min^{-1}) until 230 °C. This final temperature is maintained for 5 min. The carrier gas was premium quality N$_2$ with a flux of 1 mL min^{-1}.

Results and discussion

Theoretical calculations

Electrostatic potential calculations. With the purpose of investigate the potential use of noble metal NPs for VOC capture and retention, we conducted a DFT-D3 study using a computational model of the Ag and Au NPs and several common VOCs (see Fig. 2). In the case of the metal NPs, we used a layer of 26 atoms taken from a 282 atom NP (see Computational methods) and performed the Molecular Electrostatic Potential (MEP) surface analysis.

As noted in Fig. 3, we found positive electrostatic potential regions (located over the Ag and Au atoms), which accounted for the presence of holes, while also negative potential regions (located in between the metal atoms) confirming the presence of lumps. These positive and negative potential regions allowed the metal layers to favorably interact with both electron rich and electron poor aromatic VOCs from the point of view of electrostatics. Also, the MEP value over the holes is similar for both metal clusters (+3.5 kcal mol^{-1} in Ag26 and +3.3 kcal mol^{-1} in Au26), thus anticipating a similar VOC-NP strength upon binding to electron rich VOCs. On the other hand, the lumps present in the Ag26 cluster exhibited a more negative potential (−4.8 kcal mol^{-1}) compared to the Au26 cluster (−1.9 kcal mol^{-1}), thus expecting a stronger binding with electron poor VOCs in the case of the former.[26]

We also computed the MEP surfaces of the different VOCs used in this study (see Fig. 4) and the results obtained followed the expected trend (see Table 1). That is, the π-basicity of the ring increases on going from benzene to the methyl-substituted derivatives (toluene, o-, m- and p-xylene and 1,2,3-trimethylbenzene), ranging between −21.3 and −15.1 kcal mol^{-1}. On the other hand, in the case of 1,3,5-trifluorobenzene and hexafluorobenzene rings, the electrostatic potential showed a slightly positive value in the case of the former (+4.4 kcal mol^{-1}) while a large and positive value was obtained in the latter (+22.6 kcal mol^{-1}), as it is commonly known. Consequently, it is expected that those complexes involving 1,2,3-trimethylbenzene and o-xylene moieties obtain the most negative interaction energy values among the aromatic VOCs used. On the other hand, the hexafluorobenzene might also interact tightly with the lumps present in the metal layer owing to its positive MEP value. Lastly, the presence of methyl groups might be also important for binding, since they might be able to favorably interact with the Ag and Au layer.

Energetic study. In Fig. 5 some representative Rg–π complexes are shown involving benzene (**1**), m-xylene (**4**), hexafluorobenzene (**8**), toluene (**10**), 1,2,3-trimethylbenzene (**13**) and 1,3,5-trifluorobenzene (**15**). As noticed, in all the cases the VOC is located over the central part of the metal layer, in a parallel disposition. Also, in complexes **4**, **10** and **13** C–H···Ag and C–H···Au interactions are established, thus also contributing to the interaction energies obtained. Furthermore, the intermolecular distances between the ring centroid from the aromatic moiety and the closest metal atom are also indicated, exhibiting values beyond 3 Å, thus indicating a noncovalent contact. The interaction energies, equilibrium distances and the value of the density at the bond critical point (BCP)[43] that characterizes the Rg–π and CH–Ag/Au interactions for all complexes used herein are gathered in Table 2.

Interestingly, in all the cases attractive and moderately strong interaction energy values were obtained, ranging between −25.8 and −13.2 kcal mol^{-1}. Also, complexes involving Au26 (**9** to **16**) exhibited larger interaction energy values (ranging between −25.8 and −15.5 kcal mol^{-1}) compared to
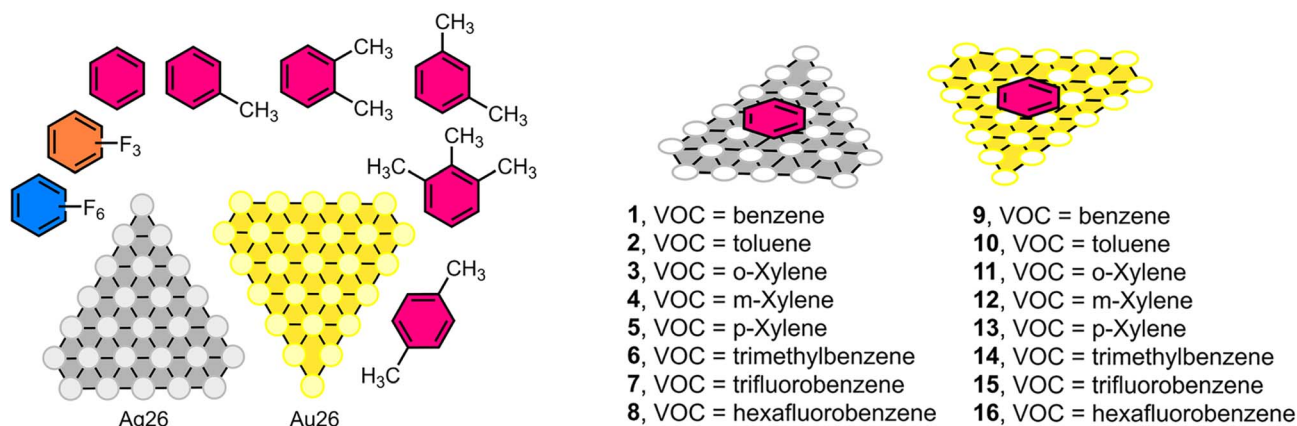

Fig. 2 Compounds and complexes used in this study.

1, VOC = benzene
2, VOC = toluene
3, VOC = o-Xylene
4, VOC = m-Xylene
5, VOC = p-Xylene
6, VOC = trimethylbenzene
7, VOC = trifluorobenzene
8, VOC = hexafluorobenzene

9, VOC = benzene
10, VOC = toluene
11, VOC = o-Xylene
12, VOC = m-Xylene
13, VOC = p-Xylene
14, VOC = trimethylbenzene
15, VOC = trifluorobenzene
16, VOC = hexafluorobenzene

25868 | *J. Mater. Chem. A*, 2023, **11**, 25865–25874

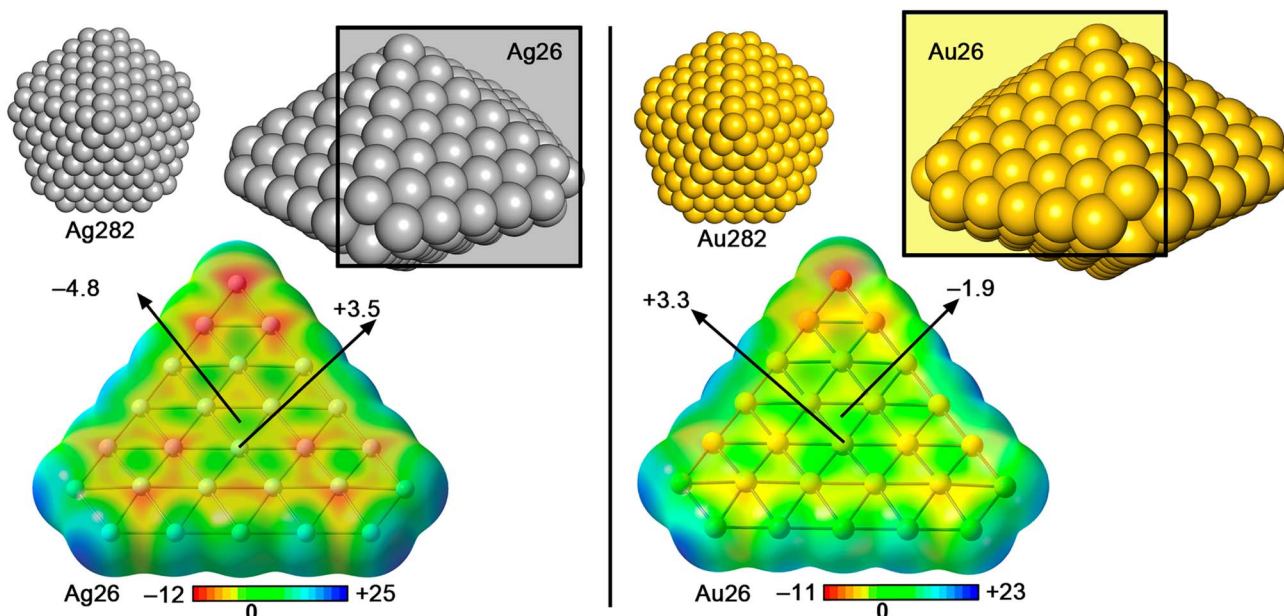This journal is © The Royal Society of Chemistry 2023

Fig. 3 Molecular Electrostatic Potential (MEP) surfaces of Ag26 and Au26 layers. The energy values given at concrete parts of the surface are in kcal mol^{-1} (0.002 a.u.).
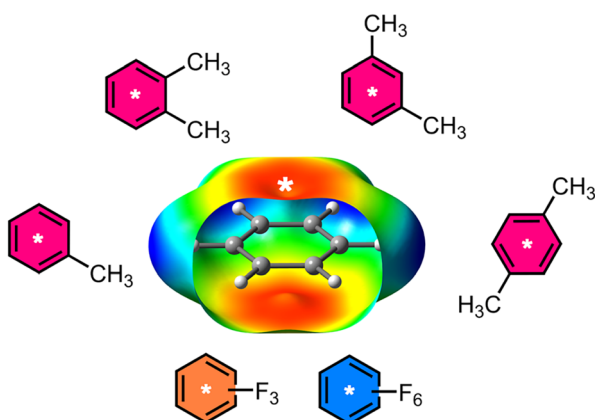

Fig. 4 MEP surface of benzene (0.002 a.u.) and schematic representation of the additional VOCs used. The values at the ring centroid (indicated with a white asterisk) as well as the MEP minima and maxima are gathered in Table 1 (kcal mol^{-1}).

Table 1 Molecular electrostatic potential values of the aromatic VOCs used in this study calculated at the center of the aromatic ring ($V_{centroid}$ in kcal mol^{-1}, 0.002 a.u.). The MEP minima and maxima (V_{min} and V_{max}, respectively) are also indicated in kcal mol^{-1}

VOC	$V_{centroid}$	V_{min}	V_{max}
Benzene	−15.1	−19	+19
Toluene	−16.3	−20	+20
o-Xylene	−20.1	−21	+21
m-Xylene	−18.9	−20	+20
p-Xylene	−18.2	−20	+20
1,2,3-Trimethylbenzene	−21.3	−21	+21
1,3,5-Trifluorobenzene	+4.4	−8	+31
Hexafluorobenzene	+22.6	−4	+26

those involving Ag26 (**1** to **8**), which resulted in an interaction strength comprised between −20.5 and −13.2 kcal mol^{-1}.

In the case of Ag26 involving complexes (**1** to **8**), complex **6** involving 1,2,3-trimethylbenzene achieved the largest interaction energy value (−20.5 kcal mol^{-1}), while complexes **7** and **8** (involving 1,3,5-trifluorobenzene and hexafluorobenzene moieties, respectively) obtained the less favorable energy values of this set (−13.5 and −13.2 kcal mol^{-1}, respectively). Additionally, the interaction energies became larger ongoing from complex **1** (involving benzene) to trimethylbenzene (complex **6**), as the number of methyl substituents is increased, in agreement with the MEP analysis discussed above. Among the three xylene derivatives, complex **3** involving o-xylene achieved a stronger interaction energy value (−19.0 kcal mol^{-1}) compared to the m- and p-derivative (−18.2 kcal mol^{-1} for both complexes **4** and **5**), also in line with the results obtained from the MEP analyses. Finally, complex **7** involving trifluorobenzene achieved a larger interaction energy value compared to complex **8** involving hexafluorobenzene, suggesting an electrostatic repulsion between the holes from the metal layer and the aromatic moiety.

For complexes involving Au26 (**9** to **16**) a similar behavior was observed, being complex **14** involving 1,2,3-trimethylbenzene the most favorable case (−25.8 kcal mol^{-1}), while complexes **15** and **16** involving the fluorinated rings achieved the less favorable interaction energy values (−16.4 and −15.5 kcal mol^{-1}, respectively). As in the case of Ag26 complexes, the interaction energies become more favorable as the number of methyl groups increased from complex **9** involving benzene to complex **14** involving 1,2,3-trimethylbenzene. Moreover, among the two fluorinated rings used, complex **15** involving 1,3,5-trifluorobenzene achieved a stronger

This journal is © The Royal Society of Chemistry 2023

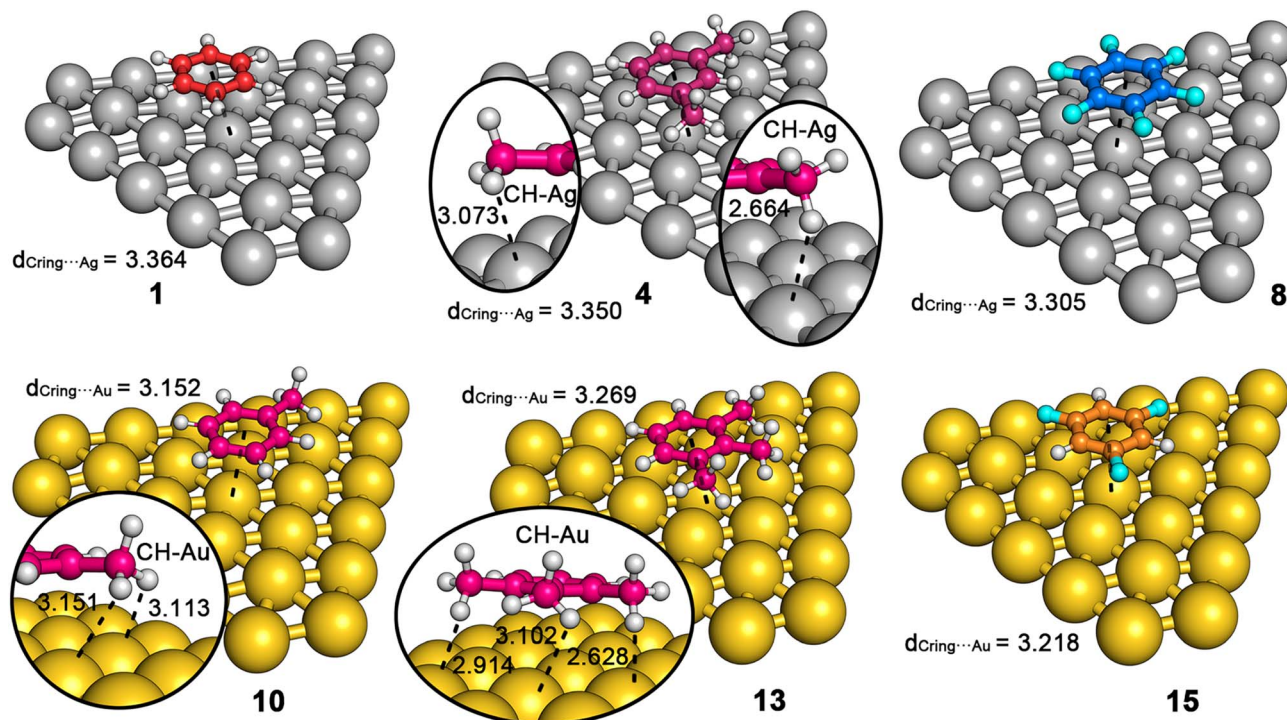J. Mater. Chem. A, 2023, **11**, 25865–25874 | **25869**

Fig. 5 Optimized geometries (PBE0-D3/def2-TZVP level of theory) of complexes **1**, **4**, **8**, **10**, **13** and **15**. Distances ($d_{\text{ring centroid}}\cdots$Ag/Au) are given in Å. Ancillary CH−Rg interactions are also indicated inside the circular parts of the image.

interaction energy (-16.4 kcal mol^{-1}) than complex **16** involving hexafluorobenzene (-15.5 kcal mol^{-1}).

Furthermore, for both sets of complexes we have estimated the energetic contribution of the CH−Ag/Au interactions, being of similar magnitude in all the cases. Lastly, it is also interesting to note that the values of the density at the bond critical point[46]

($\rho \times 10^2$) gathered in Table 2 involving the Rg−π and CH−Ag/Au interactions are generally of similar magnitude, thus indicating that both noncovalent forces are crucial for the VOC absorption process on the Ag and Au layers.

To further investigate the influence of the methyl groups on the interaction energies obtained, we have performed an Energy

Table 2 Total interaction energies and CH−Rg energetic contribution to the total interaction energy with correction for the Basis Set Superposition Error (ΔE_{BSSE} and $\Delta E_{\text{BSSE(CH−Rg)}}$ in kcal mol^{-1}), equilibrium distances (d in Å) and values of the density at the bond critical point that characterizes the Rg−π and CH−Ag/Au interactions ($\rho \times 10^2$ in a.u.) for complexes **1** to **16**

Complex	ΔE_{BSSE}	ΔE_{BSSE} (CH−Rg)^a	d	$\rho \times 10^2$ (Rg−π)^b	$\rho \times 10^2$ (CH−Ag/Au)^b
1	-14.3	—	3.364	0.78	—
2	-16.6	-2.3	3.356	0.88	0.68
3	-19.0	-2.4	3.358	0.90	0.63
4	-18.2	-1.9	3.350	0.82	0.75
5	-18.2	-1.9	3.378	0.88	0.78
6	-20.5	-2.1	3.349	0.86	0.75
7	-13.5	—	3.330	0.76	—
8	-13.2	—	3.305	0.58	—
9	-17.9	—	3.239	1.08	—
10	-21.1	-3.2	3.152	1.08	0.47
11	-23.5	-2.8	3.259	1.19	0.80
12	-23.7	-2.9	3.165	0.85	0.55
13	-23.3	-2.7	3.178	0.80	0.63
14	-25.8	-2.6	3.269	1.18	1.01
15	-16.4	—	3.218	0.80	—
16	-15.5	—	3.236	0.74	—

^{a} Values obtained as the energetic difference between complex **1** and complexes **3**, **4**, **5** and **6** in the case of the Ag26 layer and between complex **9** and complexes **10**, **11**, **12** and **13** in the case of the Au layer. The values were divided by the number of methyl groups present in the VOC structure. ^{b} Only the largest BCP density value is included.
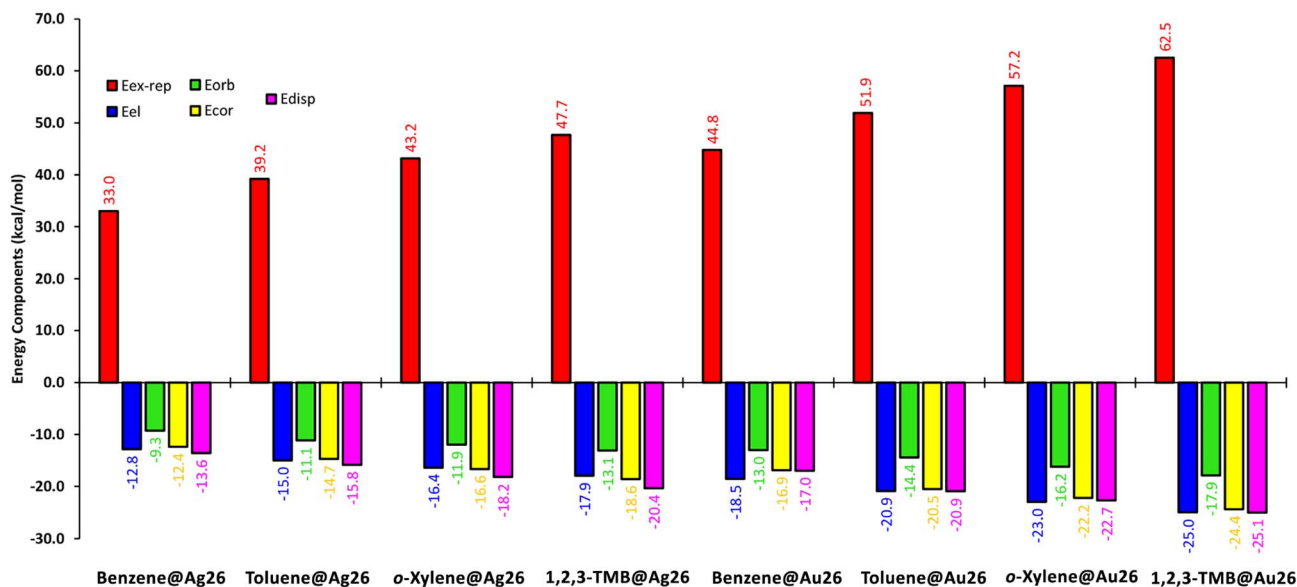
25870 | *J. Mater. Chem. A*, 2023, **11**, 25865–25874

This journal is © The Royal Society of Chemistry 2023

Fig. 6 Energy decomposition analysis into exchange-repulsion (E_{ex-rep}), electrostatics (E_{el}), orbital (E_{orb}), electron correlation (E_{cor}) and dispersion (E_{disp}) terms in kcal mol^{-1} for complexes **1** to **3**, **6**, **9** to **11** and **14**. TMB stands for trimethylbenzene.

Decomposition Analysis (EDA)[42] on eight representative examples (complexes **1** to **3**, **6**, **9** to **11** and **14**), which involved the Ag and Au layers and benzene, toluene, o-xylene and 1,2,3-trimethylbenzene. The energy partition scheme used unveiled the contribution of electrostatics, exchange-repulsion, orbital, dispersion, and electron correlation contributions (see Fig. 6). As noted, the electrostatics (E_{el}) and dispersion (E_{disp}) terms dominate the attractive contributions in both the Ag and Au set

of complexes (with the exception of complexes **3** and **6**, where the electron correlation term is larger than electrostatics) with magnitudes ranging from -25.0 to -12.8 kcal mol^{-1} (E_{el}) and from -25.1 to -13.6 kcal mol^{-1} (E_{disp}), respectively, showing a progressive increase from complexes **1** and **9** using benzene to complexes **6** and **14** using 1,2,3-trimethylbenzene.

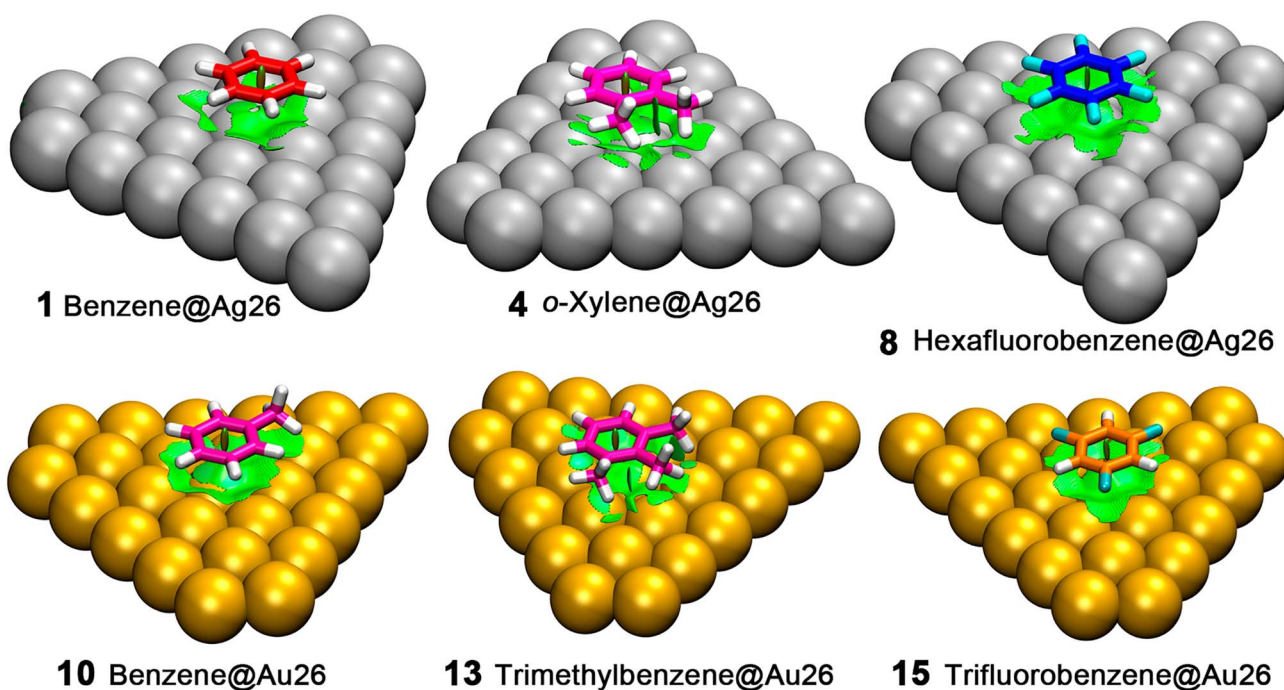In fact, in most of the computed complexes the dispersion term was slightly higher than the electrostatics (except for

Fig. 7 Non covalent interaction plot (NCIplot) analyses of complexes **1**, **4**, **8**, **10**, **13** and **15**. NCIplot color range -0.035 a.u. $\leq (sign\lambda_2)\rho \leq +0.035$ a.u. Isosurface value $|RGD| = 0.5$ and intercut parameter of 0.75.

complexes **10** and **11**). These results point to out to a shared-directing role between electrostatics and dispersive forces, in agreement with the results derived from QTAIM calculations. However, the electron correlation (E_{corr}) term also shows a very prominent role (ranging from −24.4 and −12.4 kcal mol^{-1}), exhibiting a similar magnitude to both electrostatics and dispersion contributions. Lastly, the orbital term (E_{orb}) is the less favourable contributor of all the attractive energy terms, with a magnitude comprised between −17.9 and −9.3 kcal mol^{-1}.

NCIplot and NBO analyses. A spatial analysis of the non-covalent forces present in these systems was carried out by means of NCIplot methodology, which enables the visualization in real space of non covalent forces responsible for the stabilization of the Rg–π complexes studied herein. In Fig. 7, the NCIplot analysis of complexes **1**, **4**, **8**, **10**, **13** and **15** is shown. As noted, in all the cases a greenish isosurface covering the entire aromatic moiety is located between the VOC and the Ag/Au layer, thus confirming the weak nature (noncovalent) of the Rg–π complexes. In addition, in the case of methyl-substituted aromatic systems (complexes **4**, **10** and **13**), the isosurface was extended to the region between the CH groups of the VOC and the Ag/Au atoms from the metal layer, thus characterizing ancillary CH···Ag/Au interactions.

We have also carried out NBO calculations, with particular emphasis on the second order perturbation analysis[47] on some representative complexes, owing to its usefulness when studying donor–acceptor interactions (see Table 3). As noted, in all the cases we found an orbital interaction that consists in the donation from a bonding C–C orbital (BD C–C) to unfilled s and p orbitals (s* and p*, respectively) from Ag/Au atoms, with a magnitude comprised between 4.86 and 12.44 kcal mol^{-1}. The presence of this contribution characterizes the Rg–π bonds studied herein, and agrees with that observed for previous computational studies carried out by some of us.[26]

Also, for complexes **1**, **4**, **10**, **13** and **15** we found a back-donating contribution from lone pairs (LP) belonging to the metal atom to an antibonding C–C orbital (BD* C–C) with a lower magnitude ranging between 0.36 and 1.27 kcal mol^{-1}. Finally, in the case of those complexes bearing a methyl group (**4**, **10** and **13**), an additional orbital interaction was found involving a LP from the metal atom and an antibonding C–H orbital (BD* C–H), with a magnitude encompassed between 10.54 and 27.10 kcal mol^{-1}, thus also remarking the importance of this orbital interaction to the stability of the complexes studied herein.

Experimental results

Bearing in mind the results gathered from calculations, TD experiments were conducted to evaluate the VOC absorption capacity of the Ag and Au NPs. In this regard, it is important to indicate that the lack of solvent prevented the obtention of calibration plots that allow the calculation of the absolute percentage retention for VOCs. Despite this, the percentages obtained have been calculated considering a value of 100% adsorption using commercial adsorbent tubes as a reference. In this way, the peak area of the chromatogram observed for the same VOC with the three different types of adsorbents is always compared.

In all the cases, retention is lower for Ag and Au nanoparticles than for commercial adsorbents; however, it is not always true that the actual percentage of VOC retention is 100% in the case of the commercial mixture. Therefore, the analysis of the results must be carried out considering trends and not the absolute numerical values obtained through this protocol. In Fig. 8, a diagram of the analytical process carried out is shown (see Methods above for specific details).

As it can be deduced from the results (see Table 4 below), the relative adsorption percentages of each VOC are similar for both metallic NPs, although they are slightly higher in the case of Au than Ag. Interestingly, a certain selectivity against the most electron rich rings (1,2,3-trimethylbenzene and the three xylene derivatives) was observed, leading to the highest absorption values. On the other hand, electron poor aromatic systems, such as hexafluorobenzene achieved the lowest absorption values of the study, in agreement with the behavior predicted by DFT-D3 calculations. As expected, the relative retention percentages for
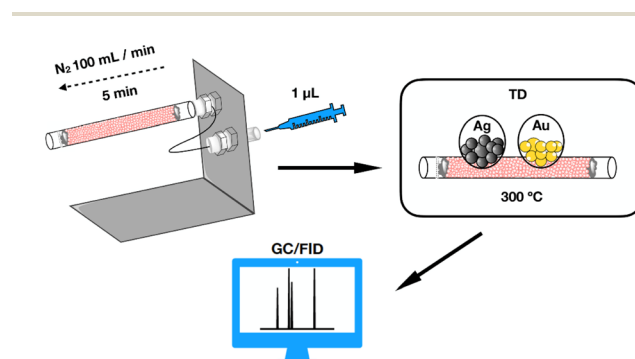
Table 3 Donor and acceptor NBOs with indication of the second-order interaction energy $E^{(2)}$ in complexes **1**, **4**, **8**, **10**, **13** and **15**. LP, BD, BD* and s* and p* stand for lone pair, bonding orbital, antibonding orbital and unfilled s and p orbitals, respectively. Energy values are in kcal mol^{-1}

Complex	Donor	Acceptor	$E^{(2)}$
1	BD C–C	s* and p*Ag	12.44
	LP Ag	BD* C–C	0.73
4	BD C–C	s* and p*Ag	9.80
	LP Ag	BD* C–C	0.36
	LP Ag	BD* C–H	10.75
8	BD C–C	s* and p*Ag	6.42
10	BD C–C	s* and p*Au	6.05
	LP Au	BD* C–C	0.99
	LP Au	BD* C–H	10.54
13	BD C–C	s* and p*Au	4.86
	LP Au	BD* C–C	1.27
	LP Au	BD* C–H	27.10
15	BD C–C	s* and p*Au	7.29
	LP Au	BD* C–C	0.44

Fig. 8 Schematic representation of the analytical procedure.

25872 | *J. Mater. Chem. A*, 2023, **11**, 25865–25874

This journal is © The Royal Society of Chemistry 2023

Table 4 Experimental results obtained following the procedure described in Fig. 8. RT, Ag% rel and Au% rel stand for retention time (RT, in minutes), AgNP absorption percentage and AuNP absorption percentage, respectively

VOC	RT	Ag% rel[a]	Au% rel[a]
Benzene	13.6	3.5 ± 0.2	5.0 ± 0.2
Toluene	17.2	11.8 ± 0.6	12.5 ± 0.6
o-Xylene	21.6	38.8 ± 1.9	42.8 ± 2.1
m-Xylene	20.7	38.2 ± 1.9	39.5 ± 2.1
p-Xylene	20.7	36.1 ± 1.9	39.6 ± 2.1
1,2,3-Trimethylbenzene	25.9	61.3 ± 3.1	70.0 ± 3.5
1,3,5-Trifluorobenzene	11.8	0.6 ± 0.1	1.2 ± 0.1
Hexafluorobenzene	11.7	2.8 ± 0.2	4.5 ± 0.2

[a] Values calculated as the arithmetic average of the mean values obtained on different analysis days. Those values with an error percentage higher than 5% have been discarded.

the three xylenes are similar, suggesting that the distribution of the substituents of the aromatic ring does not influence the retention capacity of the nanomaterial, also in line with the interaction energy values obtained (see complexes **3** to **5** and **11** to **13** in Table 2).

The notably minimal percentage of retention observed for benzene, trifluorobenzene, and hexafluorobenzene underscores the critical role of CH···metal contacts in establishing an efficacious interaction between the VOC and the nanoparticle.

Within the scope of the studied systems, the presence of methyl groups not only augments the electron-rich character of the ring, thereby reinforcing the Rg–π interaction, but also significantly contributes to anchoring the VOC onto the nanoparticle's surface.

Conclusions

In this work, we have combined theoretical calculations at the PBE0-D3/def2-TZVP level of theory with TD experiments to investigate the molecular recognition process between several VOCs and Ag and Au NPs. Computations revealed the attractive nature of the interaction, based on Rg–π bonds and CH–Ag/Au interactions. On the other hand, experimental results evidenced the noncovalent character of the VOC···metal NP interaction, showing a dependance on the NP and the VOC used.

In general, the trends observed when comparing the VOC retention time agreed with the results obtained from calculations, which pointed out to a shared director role between the Rg–π bond and the C–H···Ag/Au interaction in the capturing mechanism of VOCs. Within the scope of the systems studied herein, the presence of methyl groups not only augmented the electron-rich character of the ring, thereby reinforcing the Rg–π interaction, but also significantly contributed to anchoring the VOC onto the nanoparticle's surface through the C–H···Ag/Au contacts.

We expect the results derived from our study might be useful for the rational design of VOC capturing materials based on noble metals as well as to bring the attention of the material science community into this novel type of noncovalent bond.

Author contributions

Conflicts of interest

There are no conflicts to declare.

Acknowledgements

References

1 X. L. Cao, M. Sparling and R. Dabeka, Occurrence of 13 Volatile Organic Compounds in Foods from the Canadian Total Diet Study, *Food Addit. Contam.: Part A*, 2004, **143**, 87.
2 Y. Dumanoglu, M. Kara, H. Altiok, M. Odabasi, T. Elbir and A. Bayram, *Atmos. Environ.*, 2014, **98**, 168.
3 H. Guo, S. C. Lee, P. K. K. Louie and K. F. Ho, *Chemosphere*, 2004, **57**, 1363.
4 A. Srivastava, A. E. Joseph, S. Patil, A. More, R. C. Dixi and M. Prakash, *Atmos. Environ.*, 2005, **39**, 59.
5 K. Matsui, *Curr. Opin. Plant Biol.*, 2016, **32**, 24.
6 N. Duradeva, A. Klempien, J. K. Muhlemann and I. Kaplan, *New Phytol.*, 2013, **198**, 16.
7 S. Fischer, P. Trefz, A. Bergmann, M. Steffens, M. Ziller, W. Miekisch, J. S. Schubert, H. Köhler and P. Reinhold, *J. Breath Res.*, 2015, **14**, 027108.
8 Z. X. Zhang, Z. Jiang and W. F. Shangguan, *Catal. Today*, 2016, **264**, 270.
9 W.-L. Lau and L.-Y. Chan, *Sci. Total Environ.*, 2003, **308**, 143.
10 M. Even, M. Girard, A. Rich, C. Hutzler and A. Luch, *Front. Public Health*, 2019, **7**, 202.
11 K. L. Alford and N. Kumar, *Int. J. Environ. Res. Public Health*, 2021, **18**, 1578.
12 V. Soni., P. Singh, V. Shree and V. Goel, *Effects of VOCs on Human Health*, ed. N. Sharma, A. K. Agarwal, P. Eastwood, T. Gupta and A. P. Singh. Springer, Singapore, 2018.
13 Y. Bo, H. Cai and S. D. Xie, *Atmos. Chem. Phys. Discuss.*, 2008, **8**, 11519.
14 H. T. Liao, C. C.-K. Chou, J. C. Chow, J. G. Watson, P. K. Hopke and C. F. Wu, *Environ. Pollut.*, 2015, **205**, 121.
15 K. Q. Qiu, L. X. Yang, J. M. Lin, P. Wang, Y. Yang, D. Q. Ye and L. M. Wang, *Atmos. Environ.*, 2014, **86**, 102.
16 J. N. Zhang, J. F. Xiao, X. F. Chen, X. M. Liang, L. Y. Fan and D. Q. Ye, *J. Environ. Sci.*, 2018, **69**, 155.
17 E. Cetin, M. Odabasi and R. Seyfioglu, *Sci. Total Environ.*, 2003, **312**, 103.

This journal is © The Royal Society of Chemistry 2023

J. Mater. Chem. A, 2023, **11**, 25865–25874 | **25873**

18 D. Nuvolone, D. Petri and F. Voller, *Environ. Sci. Pollut. Res. Int.*, 2018, **25**, 8074.

19 A. C. Pozzer, P. A. Gómez and J. Weiss, *Sci. Total Environ.*, 2022, **838**, 156155.

20 https://www.epa.gov/stationary-sources-air-pollution/consumer-products-national-volatile-organic-compound-emission, accessed on 25/06/2023.

21 https://www.uscoatings.com/blog/voc-regulations-and-what-they-mean-for-manufacturers/, accessed on 25/06/2023.

22 https://tbfenvironmental.com/vocmir-regulations/voc-and-mir-regulations-by-jurisdiction/us-environmental-protection-agency/, accessed on 25/06/2023.

23 J. H. Stenlid and T. Brinck, *J. Am. Chem. Soc.*, 2017, **139**, 11012.

24 J. Joy and E. D. Jemmis, *Inorg. Chem.*, 2017, **56**, 1132.

25 J. H. Stenlid, A. J. Johansson and T. Brinck, *Phys. Chem. Chem. Phys.*, 2018, **20**, 2676.

26 A. Frontera and A. Bauzá, *Chem.–Eur. J.*, 2018, **24**, 7228.

27 M. N. Piña, P. Rodríguez, M. S. Gutiérrez, D. Quiñonero, J. Morey and A. Frontera, *Chem.–Eur. J.*, 2018, **24**, 12820.

28 M. N. Piña, M. S. Rodríguez, M. Penagos, P. Duel, A. León, J. Morey, D. Quiñonero and A. Frontera, *RSC Adv.*, 2019, **9**, 24184.

29 C. Adamo and V. Barone, *J. Chem. Phys.*, 1999, **110**, 6158.

30 M. Ernzerhof and G. E. Scuseria, *J. Chem. Phys.*, 1999, **110**, 5029.

31 S. Grimme, J. Antony, S. Ehrlich and H. Krieg, *J. Chem. Phys.*, 2010, **132**, 154104.

32 A. Schäfer, H. Horn and R. Ahlrichs, *J. Chem. Phys.*, 1992, **97**, 2571.

33 S. G. Balasubramani, G. P. Chen, S. Coriani, M. Diedenhofen, M. S. Frank, Y. J. Franzke, F. Furche, R. Grotjahn, M. E. Harding, C. Hättig, A. Hellweg, B. Helmich-Paris, C. Holzer, U. Huniar, M. Kaupp, A. M. Khah, S. K. Khani, T. Müller, F. Mack, B. D. Nguyen, S. M. Parker, E. Perlt, D. Rappoport, K. Reiter, S. Roy, M. Rückert, G. Schmitz, M. Sierka, E. Tapavicza, D. P. Tew, C. van Wüllen, V. K. Voora, F. Weigend, A. Wodyński and J. M. Yu, *J. Chem. Phys.*, 2020, **152**, 184107.

34 K. Sawabe and A. Satsuma, *ACS Omega*, 2022, **7**, 4405.

35 S. F. Boys and F. Bernardi, *Mol. Phys.*, 1970, **19**, 553.

36 M. J. Frisch, G. W. Trucks, H. B. Schlegel, G. E. Scuseria, M. A. Robb, J. R. Cheeseman, G. Scalmani, V. Barone, G. A. Petersson, H. Nakatsuji, X. Li, M. Caricato, A. V. Marenich, J. Bloino, B. G. Janesko, R. Gomperts, B. Mennucci, H. P. Hratchian, J. V. Ortiz, A. F. Izmaylov, J. L. Sonnenberg, D. Williams-Young, F. Ding, F. Lipparini, F. Egidi, J. Goings, B. Peng, A. Petrone, T. Henderson, D. Ranasinghe, V. G. Zakrzewski, J. Gao, N. Rega, G. Zheng, W. Liang, M. Hada, M. Ehara, K. Toyota, R. Fukuda, J. Hasegawa, M. Ishida, T. Nakajima, Y. Honda, O. Kitao, H. Nakai, T. Vreven, K. Throssell, J. A. Montgomery Jr, J. E. Peralta, F. Ogliaro, M. J. Bearpark, J. J. Heyd, E. N. Brothers, K. N. Kudin, V. N. Staroverov, T. A. Keith, R. Kobayashi, J. Normand, K. Raghavachari, A. P. Rendell, J. C. Burant, S. S. Iyengar, J. Tomasi, M. Cossi, J. M. Millam, M. Klene, C. Adamo, R. Cammi, J. W. Ochterski, R. L. Martin, K. Morokuma, O. Farkas, J. B. Foresman and D. J. Fox, *Gaussian 16, Revision C.01*, Gaussian, Inc., Wallingford CT, 2016.

37 R. Dennington, T. A. Keith and J. M. Millam, *GaussView, Version 6*, Semichem Inc., Shawnee Mission, KS, USA, 2016.

38 T. A. Keith, *AIMAll (Version 19.10.12)*, TK Gristmill Software, Overland Park KS, USA, 2019.

39 E. D. Glendening, J. K. Badenhoop, A. E. Reed, J. E. Carpenter, J. A. Bohmann, C. M. Morales, P. Karafiloglou, C. R. Landis and F. Weinhold, *Theoretical Chemistry Institute*, University of Wisconsin, Madison, 2018.

40 L. Zhao and M. von Hopffgarten, *Wiley Interdiscip. Rev.: Comput. Mol. Sci.*, 2018, **8**, e1345.

41 K. Kitaura and K. Morokuma, *Int. J. Quantum Chem.*, 1976, **10**, 325.

42 J. Contreras-García, E. R. Johnson, S. Keinan, R. Chaudret, J.-P. Piquemal, D. N. Beratan and W. Yang, *J. Chem. Theory Comput.*, 2011, **7**, 625.

43 W. Humphrey, A. Dalke and K. Schulten, *J. Mol. Graphics*, 1996, **14**, 33.

44 S. D. Solomon, M. Bahadory, S. Jeyarajasingam, S. A. Rutkowky and C. Boritz, *J. Chem. Educ.*, 2007, **84**, 322.

45 A. Ribes, G. Carrera, E. Gallego, X. Roca, M. J. Berenguer and X. J. Guardino, *J. Chromatogr. A*, 2007, **1140**, 44.

46 R. F. W. Bader, *Acc. Chem. Res.*, 1985, **18**, 9.

47 F. Weinhold, C. R. Landis and E. D. Glendening, *Int. Rev. Phys. Chem.*, 2016, **35**, 399.

25874 | *J. Mater. Chem. A*, 2023, **11**, 25865–25874

This journal is © The Royal Society of Chemistry 2023